

Low-temperature phase transition in polar semimetal T_d -MoTe₂ probed by nonreciprocal transport

Yuki M. Itahashi ¹, Yamato Nohara ¹, Toshiya Ideue ^{1,*}, Tomoki Akiba,² Hidefumi Takahashi ²,
Shintaro Ishiwata ² and Yoshihiro Iwasa ^{1,3}

¹Quantum-Phase Electronics Center (QPEC) and Department of Applied Physics, The University of Tokyo, Tokyo 113-8656, Japan

²Division of Materials Physics, Graduate School of Engineering Science, Osaka University, Toyonaka 560-8531, Japan

³RIKEN Center for Emergent Matter Science (CEMS), Wako 351-0198, Japan



(Received 3 November 2022; accepted 23 March 2023; published 2 May 2023)

We studied the nonreciprocal transport of layered MoTe₂, which undergoes a structural transition from centrosymmetric to the noncentrosymmetric polar phase. Careful inspections of the temperature-dependent resistance showed an occurrence of additional phase transition at around $T^* = 50$ K inside the noncentrosymmetric polar phase. We found that the nonreciprocal signal emerges below T^* , associated with the filling of the hole pocket. The present result suggests that the mechanism of the nonreciprocal transport is significantly distinct from that in simple polar semiconductors but is highly sensitive to the small hole pocket buried in the major carriers in semimetals.

DOI: [10.1103/PhysRevResearch.5.L022022](https://doi.org/10.1103/PhysRevResearch.5.L022022)

Broken inversion symmetry in two-dimensional van der Waals crystals plays crucial roles in their emergent optical and transport properties. So far, symmetry breaking along the in-plane direction of two-dimensional crystals has been focused on in many studies. For example, semiconducting monolayer transition-metal dichalcogenides (TMDs) such as MoS₂ and WSe₂ have characteristic valley-related optical and transport properties originating from the noncentrosymmetric threefold rotational symmetry [1]. Another example is mono- or few-layer WTe₂ [2,3], where only one mirror plane remains and thus the nonlinear anomalous Hall effect appears reflecting this in-plane low symmetry. Recently, the reduction of the in-plane symmetry was found to occur by the formation of van der Waals heterointerfaces, associated with characteristic nonlinear responses [4,5].

As well as in-plane symmetry of two-dimensional van der Waals nanostructures, the out-of-plane inversion symmetry breaking caused by the unique crystal structure or stacking sequence of two-dimensional materials are also attracting much attention in recent days. In bilayer hexagonal boron nitride or TMDs [6,7], stacking-dependent out-of-plane electric polarization has been reported. In these materials, ferroelectricity is caused by the artificially engineered stacking. Remarkably, several polytypes of TMDs such as 3R or T_d structures naturally host the out-of-plane polarity [8,9]. Especially, T_d -MoTe₂ shows a reversible thermally driven phase transition between centrosymmetric $1T'$ phase and non-

centrosymmetric T_d phase [10–13], providing an ideal material platform for studying the polarity-dependent emergent properties.

With decreasing the temperature, sliding of two-dimensional layers and displacement of Te atoms cause the modulation of the unit cell and resultant symmetry change, leading to the phase transition from centrosymmetric $1T'$ to polar T_d structure [Fig. 1(a)]. To detect the effect of out-of-plane polarization in layered materials, observation of the out-of-plane electric or optoelectric properties are widely used [14,15]. However, such measurements could be affected by extrinsic effects such as interfacial scattering and effect of the device asymmetry. In contrast, bulk rectification effect (second-harmonic magnetotransport) [16–19] will provide the detailed information of exotic electronic structure originating from out-of-plane polarization via in-plane transport measurement, thus being suitable for detecting the effect of symmetry breaking in the present system.

In this Letter, we studied the first- and second-harmonic transport in noncentrosymmetric phase of MoTe₂. We found an anomalous behavior in temperature (T) dependences of the first-harmonic resistivity and its temperature derivative around $T = 50$ K, implying the occurrence of an additional phase transition in low-temperature noncentrosymmetric phase of MoTe₂, which has been considered as the Weyl semimetallic phase. Importantly, nonreciprocal transport (i.e., nonlinear longitudinal and transverse magnetotransport) appears only below this transition temperature ($T^* = 50$ K) and becomes negligibly small above T^* , although MoTe₂ should have the polar crystal symmetry above and below T^* . We also found that this phase transition is accompanied by the carrier compensation driven by the emerging hole pocket, which indicates that nonreciprocal transport is largely enhanced by the scattering process between electrons and holes in the low-temperature phase. The present results indicate

*ideue@ap.t.u-tokyo.ac.jp

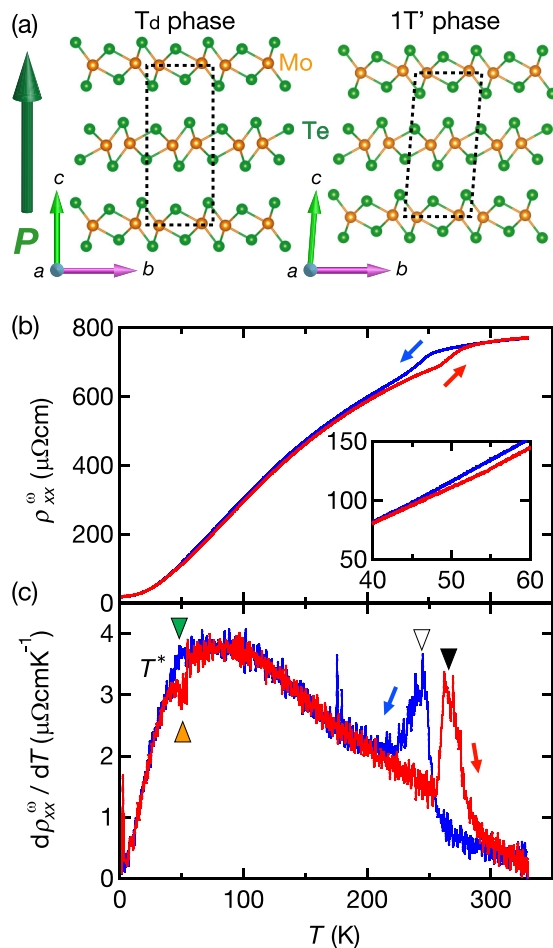


FIG. 1. (a) Schematic crystal structure of 1T' (right) and T_d (left) MoTe₂. Boxes with dashed line indicate the unit cell. 1T' phase is centrosymmetric and T_d phase has a noncentrosymmetric crystal structure with an out-of-plane polarity. (b) Longitudinal first-harmonic resistivity ρ_{xx}^{ω} as a function of temperature T for sample 1 (bulk with $t \sim 30 \mu\text{m}$). Inset shows the magnification of ρ_{xx}^{ω} around $T = 50 \text{ K}$. (c) Temperature derivative of ρ_{xx}^{ω} ($d\rho_{xx}^{\omega}/dT$) for sample 1. White and black triangles indicate peak positions in cooling and heating scan, respectively, which correspond to the noncentrosymmetric-to-centrosymmetric phase transition. Green and orange triangles exhibit the peak and dip positions in cooling and heating scan, respectively, which imply another phase transition inside the noncentrosymmetric phase. In (b) and (c), we scanned temperature by 1 K/min.

that nonlinear transport is a highly sensitive probe of electronic structure and charge dynamics of noncentrosymmetric semimetals.

Single crystals of 1T'–MoTe₂ were synthesized via a chemical vapor transport technique (see Supplemental Material [20]). The obtained 1T'–MoTe₂ single crystals were exfoliated into thin flakes using the Scotch tape method, and the flakes were transferred onto a Si–SiO₂ substrate. The thickness of the exfoliated flakes was measured by using atomic force microscopy. A Hall bar configuration was fabricated on the flakes with Au (150-nm)/Ti (9-nm) electrodes. For the bulk sample, on the other hand, we once exfoliate the bulk by using Scotch tape to obtain the fresh surface and

deposited Au (100-nm)/Ti (10-nm) electrodes defined by the stencil.

Then, we measured the first- and second-harmonic electric transport by a standard lock-in technique (see Supplemental Material [20]), in both bulk (\sim millimeter size) and exfoliated flake samples (micrometer size) of single-crystal MoTe₂. By using micrometer-size devices, we can obtain the monodomain sample and high current density, which is advantageous for investigating the second-order nonlinear transport properties reflecting the out-of-plane polarization. In fact, the typical domain size of MoTe₂ is estimated to be around $100 \mu\text{m}$ [21] and bulk (millimeter-size) sample with Hall bar configuration did not show the discernible second-harmonic response probably due to the multidomain and small current density (see Supplemental Material [20]). Also, we can determine the crystal orientation of bulk and exfoliated thin flakes by their shape [22,23]. In the following, we mainly focus on the devices with the current along the a direction (Mo–Mo zigzag chains), unless stated otherwise. It is noted that the second-harmonic transport reflecting the out-of-plane polarity similarly appears whether in-plane current direction is parallel to the a or b axis.

First, we focus on the first-harmonic (linear) resistivity in bulk MoTe₂ with the thickness $t \sim 30 \mu\text{m}$ (sample 1). Figure 1(b) shows the first-harmonic resistivity (ρ_{xx}^{ω}) as a function of temperature. The value of residual resistivity ratio (RRR) in sample 1 is 42, which is consistent with the previous studies [24,25]. Around $T = 250 \text{ K}$, we observed the kinks and hysteresis loop indicating the first-order phase transition. Interestingly, the hysteresis does not close below 250 K in Fig. 1(b) but continues down to around $T^* = 50 \text{ K}$, as shown in the inset of Fig. 1(b). When the hysteresis loop closes near T^* , we found a resistance anomaly and resultant slight difference between cooling and heating scans above T^* . Figure 1(c) shows the temperature derivative of ρ_{xx}^{ω} ($d\rho_{xx}^{\omega}/dT$). In addition to the peak structures around $T = 250 \text{ K}$ (black and white triangles), we can see the peak (dip) structure in the cooling (heating) scan around $T^* = 50 \text{ K}$, as shown by a green (orange) triangle. The observed anomaly in ρ_{xx}^{ω} and its temperature derivative in a bulk sample implies the existence of additional phase transition inside the noncentrosymmetric phase of MoTe₂.

This behavior of the first-harmonic resistivity is also observed in exfoliated flake samples. Figure 2(a) shows ρ_{xx}^{ω} normalized by that at $T = 300 \text{ K}$, as a function of temperature T in samples 2, 3, 4, and 5 together with bulk sample 1. Here, samples 2, 3, 4, and 5 are exfoliated flakes with $t = 140, 125, 52, \text{ and } 4.5 \text{ nm}$, respectively. Resistivity of exfoliated flake samples also show a hysteresis around $T = 250 \text{ K}$. In thin samples, the hysteresis loop around the structural phase transition around $T = 250 \text{ K}$ becomes broader due to the thinning effect [12], but the loop is more clearly seen down to 50 K . We can still see the clear anomaly of ρ_{xx}^{ω} [Figs. 2(b) and 2(c)] and resultant obvious peak and dip structures in $d\rho_{xx}^{\omega}/dT$ [Figs. 2(d) and 2(e)], similarly to the bulk sample. This anomaly is observed in all samples measured (see Supplemental Material [20]). Importantly, the cooling scan shows a peak, whereas the heating scan exhibits a dip structure of $d\rho_{xx}^{\omega}/dT$. This hysteretic behavior is distinct from the typical behavior of the first-order phase transition, indicating

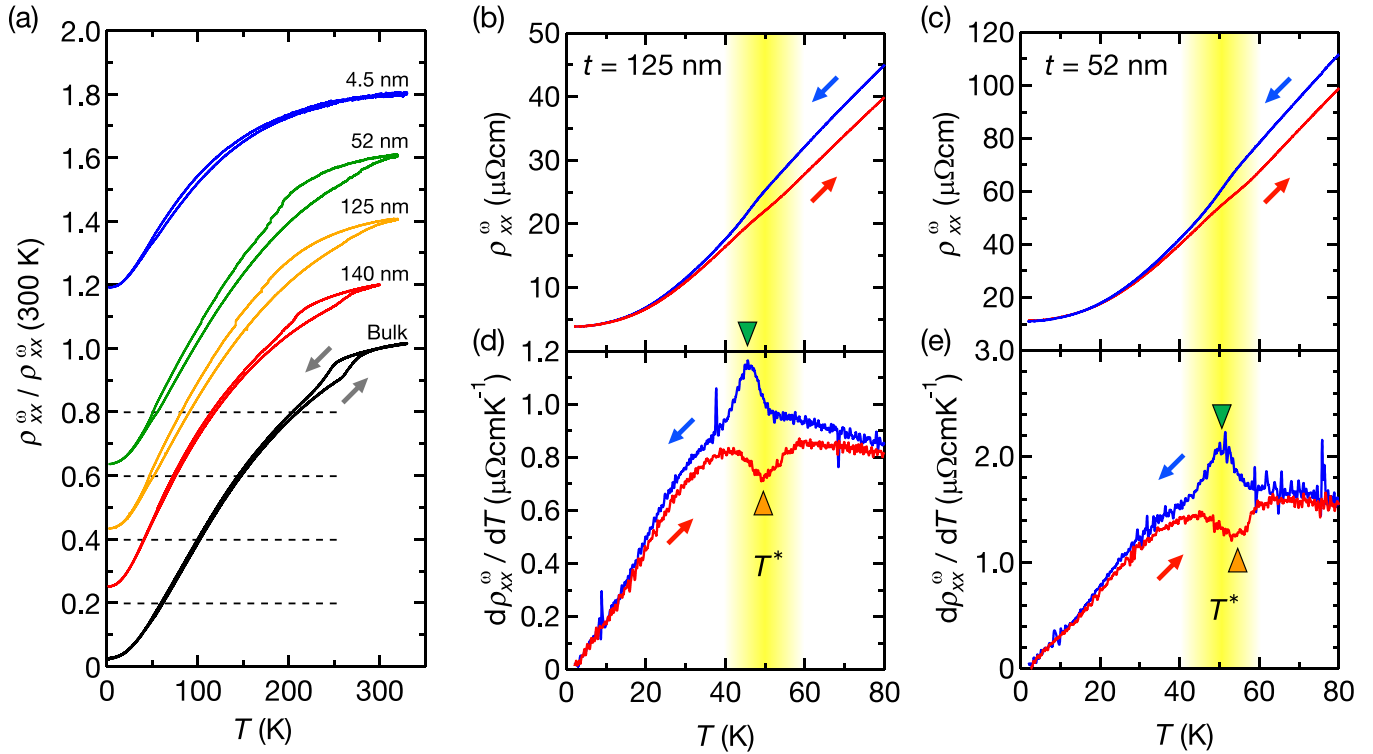


FIG. 2. (a) Longitudinal first-harmonic resistivity ρ_{xx}^{ω} normalized by that at $T = 300$ K, as a function of T in sample 1 (black, bulk with $t \sim 30 \mu\text{m}$), 2 (red, $t = 140$ nm), 3 (yellow, $t = 125$ nm), 4 (green, $t = 52$ nm), and 5 (blue, $t = 4.5$ nm). Each curve is shifted vertically by 0.2 for clarity. (b), (c) Longitudinal first-harmonic resistivity ρ_{xx}^{ω} as a function of temperature in samples 3 [(b), $t = 125$ nm] and 4 [(c), $t = 52$ nm]. (d), (e) Temperature derivative of ρ_{xx}^{ω} ($d\rho_{xx}^{\omega}/dT$) in samples 3 (d) and 4 (e). Green and orange triangles show the peak and dip positions in down and up scans, respectively. In (a)–(e), we scanned temperature by 1 K/min.

different structural or electronic states between the cooling and heating processes above T^* . Recently, the intermediate phase between the $1T'$ phase and (ordered) T_d phase has been discussed [26,27]. In this intermediate state, the $1T'$ and T_d structures are mixed, showing both the $1T'$ and T_d nature. The hysteretic behavior in ρ_{xx}^{ω} and $d\rho_{xx}^{\omega}/dT$ might come from the transition between mixed $1T'/T_d$ phase and ordered T_d phase. It should be noted that both mixed $1T'/T_d$ phase and ordered T_d phase are noncentrosymmetric and nonreciprocal transport is expected to occur in terms of symmetry.

Next, we measured the nonlinear transport, which is a sensitive probe of the crystal and electronic structure. In polar systems, nonlinear voltages ($V_x^{2\omega}$ and $V_y^{2\omega}$) are generally expected when applied current is perpendicular (configuration A) and parallel (configuration B) to the magnetic field as shown in Figs. 3(a) and 3(b), respectively. Figures 3(c) and 3(d) show the second-harmonic longitudinal resistivity $\rho_{xx}^{2\omega}$ and transverse resistivity $\rho_{yx}^{2\omega}$ as a function of magnetic field B in configuration A (red/light blue) and B (pink/blue), respectively, at $T = 2$ K in sample 3. In configuration A (B), finite B -linear $\rho_{xx}^{2\omega}$ ($\rho_{yx}^{2\omega}$) is observed, with indiscernible signals in the other direction. These results are consistent with the above symmetry argument in polar phase.

To investigate the relationship between the nonlinear transport and the phase transition in low-temperature phase discussed above, we measured the temperature dependence of the second-harmonic resistivity. Figure 4(a) shows $\rho_{yx}^{2\omega}$ (left) and ρ_{xx}^{ω} (right) as a function of T . $\rho_{yx}^{2\omega}$ becomes negligibly

small above 70 K, which is much lower than the temperature of noncentrosymmetric-to-centrosymmetric phase transition (around 200 K in 100-nm-thickness flakes estimated by Raman shift [12]). Instead, this onset temperature of the second-harmonic resistances is close to T^* . This behavior is distinct from the nonlinear magnetotransport in WTe_2 [17], where nonlinear signals show the temperature-induced sign reversal reflecting the shape of Fermi surface, and persist up to the room temperature. We also notice the hysteresis in $\rho^{2\omega}$, which might imply the first-order nature of the phase transition at T^* .

We now consider the origin of nonreciprocal transport observed only in low-temperature region of noncentrosymmetric phase. According to the recent studies, possible additional phase transition in low temperature phase (~ 60 K) has been discussed in Raman measurement [28] and also captured as a dramatic change in several physical properties such as magnetoresistance, (planar) Hall resistance, circular photogalvanic effect, and heat capacity [29–35]. Especially, it is known that Hall resistivity shows the abrupt change around this temperature region [29,30]. Figure 4(b) shows the temperature dependence of ρ_{yx}^{ω} at $B = 8$ T in sample 3 ($t = 131$ nm), which has almost the same thickness as sample 5. It shows the increase around $T^* = 50$ K similarly to previous studies [29,30]. Since it is well known that MoTe_2 is a semimetal with both electrons and holes, we extracted electron and hole carrier densities from ρ_{yx}^{ω} vs B and ρ_{xx}^{ω} vs B curves by alternately fitting them with two-carrier model [36,37] (see Supplemental

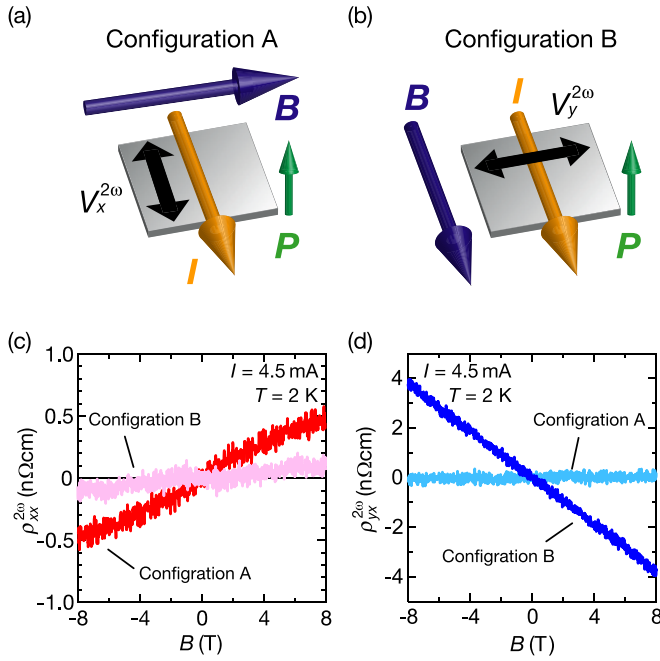


FIG. 3. (a), (b) Schematic images of two different measurement configurations for observing nonlinear transport. In polar crystals, second-harmonic longitudinal (transverse) voltage $V_x^{2\omega}$ ($V_y^{2\omega}$) is expected to appear when applied magnetic field B is perpendicular (parallel) to the applied current I . (c) Second-harmonic longitudinal resistivity $\rho_{xx}^{2\omega}$ as a function of in-plane B perpendicular (red) or parallel (pink) to I . The applied current was 4.5 mA. (d) Second-harmonic transverse resistivity $\rho_{yx}^{2\omega}$ as a function of in-plane B perpendicular (light blue) or parallel (blue) to I . The applied current was 4.5 mA. $\rho_{xx}^{2\omega}$ and $\rho_{yx}^{2\omega}$ are antisymmetrized as a function of B (see Supplemental Material [20]).

Material [20]). ρ_{yx}^{ω} and ρ_{xx}^{ω} are written as

$$\rho_{yx}^{\omega}(B) = \frac{B (n_h \mu_h^2 - n_e \mu_e^2) + \mu_h^2 \mu_e^2 (n_h - n_e) B^2}{e (n_h \mu_h + n_e \mu_e)^2 + \mu_h^2 \mu_e^2 (n_h - n_e)^2 B^2}, \quad (1)$$

and

$$\rho_{xx}^{\omega}(B) = \frac{1}{e} \frac{(n_h \mu_h + n_e \mu_e) + \mu_e \mu_h (n_e \mu_h + n_h \mu_e) B^2}{(n_h \mu_h + n_e \mu_e)^2 + \mu_h^2 \mu_e^2 (n_h - n_e)^2 B^2}, \quad (2)$$

respectively. Here, n_h (n_e) and μ_h (μ_e) are the carrier density and the mobility of holes (electrons), respectively. Figure 4(c) depicts n_h and n_e as a function of temperature. With decreasing the temperature, n_e does not change so much, showing the slight decrease. In contrast, n_h drastically changes and shows the rapid increase around $T^* = 50$ K, which results in the carrier compensation below 40 K. According to the previous study, this behavior can be understood as the growth of hole pocket around the Γ point in the low-temperature region [Fig. 4(d)], which is not directly related to the Weyl point [29,38,39]. We assume that this change in carrier densities is closely related to the phase transition between mixed $1T'/T_d$ phase and ordered T_d phase mentioned above. Figures 4(a)–4(c) indicate that the nonreciprocal transport and the development of the hole pocket occur nearly at the transition temperature found, T^* . In other words, the nonreciprocal transport increases along with the increase of hole carrier density with lowering temperature. To clearly see this

situation, we plot $\rho_{yx}^{2\omega}$ and $\rho_{xx}^{2\omega}$ as a function of n_h [Fig. 4(e)]. It seems that the transition from mixed $1T'/T_d$ phase to ordered T_d phase [Fig. 4(f)] directly causes the emergence of nonreciprocal transport. However, the sudden emergence of nonreciprocal signals around $T = 50$ K cannot be explained just by this transition because nonlinear signals should appear even in the mixed phase in which inversion symmetry is broken. Thus, we believe that the electronic structure change (i.e., increase in hole density) associated with that transition plays a crucial role in the emergence of nonreciprocal transport in MoTe_2 .

In the previous study of bulk polar semiconductor BiTeBr , the deformation of Rashba-type spin-splitting band under the in-plane magnetic field causes the nonlinear transport [16]. In this case, the nonlinear signals increase with decreasing the carrier density since the effect of band deformation becomes dominant in the bottom of the conduction band. In contrast, the second-order nonlinear transport of MoTe_2 increases in accord with the development of the hole pocket. This trend is opposite from that in BiTeBr , implying a distinct origin of the nonreciprocal transport in multicarrier semimetals. In semimetals, electrons and holes are coexisting, and scattering process between them may contribute to the nonreciprocal transport. There is a possibility that this scattering process between carriers in the different Fermi surfaces is more sensitive to the symmetry breaking than that in one simple Fermi surface. If this is the case, nonreciprocal transport can be a powerful probe of small Fermi pocket buried in the large Fermi surface of majority carriers and related Lifshitz transition, which is normally difficult to estimate by the linear transport coefficient. Although theoretical explanation of the above scenario and quantitative discussion of the observed nonreciprocal transport remains to be further pursued in the future, the present results provide an insight into multicarrier effect on the nonreciprocal transport, offering a direction of the nonlinear transport studies.

In summary, we investigated the first- and second-harmonic resistivity in MoTe_2 . We found the anomaly in the first-harmonic resistivity and its temperature derivative around $T^* = 50$ K, implying the additional phase transition in polar-phase MoTe_2 . At the lowest temperature, we observed the nonlinear longitudinal and transverse magnetoresistivity, which is fully consistent with the polar symmetry. With increasing the temperature, the nonreciprocal signals disappear at T^* , which is much lower than the well-established phase transition of noncentrosymmetric-to-centrosymmetric phase transition. The appearance of the nonreciprocal signals seems to be accompanied by the development of hole carrier pocket, which is associated with the transition between mixed $1T'/T_d$ phase and ordered T_d phase. We suppose that the scattering in developed hole pocket below T^* might be a key ingredient of the nonreciprocal transport in Weyl semimetallic T_d - MoTe_2 . The present results indicate that nonreciprocal transport can be a powerful probe of a phase transition in semimetals.

We thank N. Nagaosa and H. Ishizuka for fruitful discussions. Y.M.I. was supported by JSPS KAKENHI Grant No. JP22K20352 and a grant from Murata Science Foundation. T.I. was supported by JSPS KAKENHI Grants

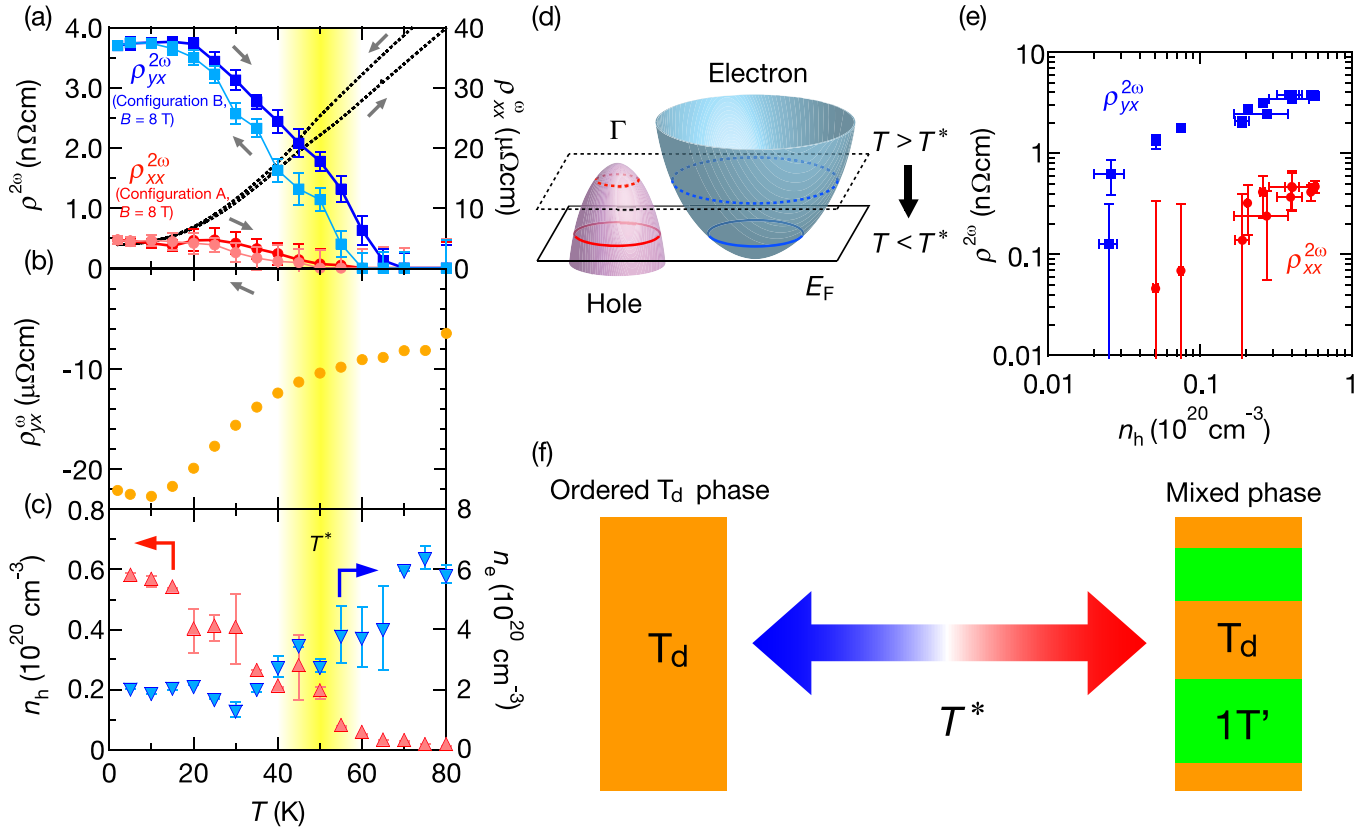


FIG. 4. (a) Second-harmonic resistivity ($\rho^{2\omega}$, left) and first-harmonic longitudinal resistivity (ρ_{xx}^{ω} , right) in sample 3 at $I = 0.05$ mA. Longitudinal ($\rho_{xx}^{2\omega}$, red and pink circles) and transverse ($\rho_{yx}^{2\omega}$, blue and light blue squares) second-harmonic resistivities are measured at $B = 8$ T. Longitudinal first-harmonic resistivity (ρ_{xx}^{ω} , dashed black line) is measured at $B = 0$ T. Error bars indicate the uncertainty of the signals estimated from magnetic field dependence of the second-harmonic signals at each temperature. (b) Transverse first-harmonic resistivity (Hall resistivity, ρ_{yx}^{ω}) at $I = 0.05$ mA and $B = 8$ T, extracted from ρ_{yx}^{ω} vs B curves at each temperature. The ρ_{yx}^{ω} vs B curves were measured in the heating process. (c) Electron density n_e (light blue down-pointing triangles) and hole density n_h (pink up-pointing triangles) extracted from the two-carrier model fitting of ρ_{yx}^{ω} vs B and ρ_{xx}^{ω} vs B curves at each temperature. Error bars indicate the uncertainty of the carrier densities obtained from the fitting results of ρ_{yx}^{ω} vs B and ρ_{xx}^{ω} vs B curves at each temperature. (d) Schematic image of the band structure in nonsymmorphic phase of MoTe₂. With decreasing the temperature across T^* , hole pocket develops, causing the carrier compensation. (e) $\rho^{2\omega}$ vs hole density n_h . Red circles and blue squares indicate $\rho_{xx}^{2\omega}$ and $\rho_{yx}^{2\omega}$, respectively. Both $\rho_{xx}^{2\omega}$ and $\rho_{yx}^{2\omega}$ increase in accordance with the development of the hole pocket. (f) Schematics of ordered T_d phase and mixed $1T'/T_d$ phase. At low temperature below T^* , the entire crystal becomes T_d structure, and this phase is called ordered T_d phase. However, between ordered T_d phase and $1T'$ phase, there is an intermediate state, where T_d and $1T'$ structures are mixed. This phase is called mixed $1T'/T_d$ phase. Phase boundary between the ordered T_d phase and mixed $1T'/T_d$ phase might be T^* . This transition might cause the hysteretic behavior in resistance and might be associated with the increase in the hole density around T^* .

No. JP19H01819 and No. JP18H04216, JST PRESTO (JP-MJPR19L1) and a grant from Yazaki Memorial Foundation for Science and Technology. S.I. was supported by JSPS

KAKENHI Grant No. JP22H00343. This work was supported by JSPS KAKENHI Grant No. JP19H05602 and the A3 Foresight Program.

- [1] K. F. Mak, K. L. McGill, J. Park, and P. L. McEuen, The valley Hall effect in MoS₂ transistors, *Science* **344**, 1489 (2014).
- [2] Q. Ma *et al.*, Observation of the nonlinear Hall effect under time-reversal-symmetric conditions, *Nature (London)* **565**, 337 (2019).
- [3] K. Kang, T. Li, E. Sohn, J. Shan, and K. F. Mak, Nonlinear anomalous Hall effect in few-layer WTe₂, *Nat. Mater.* **18**, 324 (2019).

- [4] T. Akamatsu *et al.*, A van Der Waals interface that creates in-plane polarization and a spontaneous photovoltaic effect, *Science* **372**, 68 (2021).
- [5] S. Hubmann, P. Soul, G. Di Battista, M. Hild, K. Watanabe, T. Taniguchi, D. K. Efetov, and S. D. Ganichev, Nonlinear intensity dependence of photogalvanics and photoconductance induced by terahertz laser radiation in twisted bilayer graphene close to magic angle, *Phys. Rev. Mater.* **6**, 024003 (2022).

- [6] K. Yasuda, X. Wang, K. Watanabe, T. Taniguchi, and P. Jarillo-Herrero, Stacking-engineered ferroelectricity in bilayer boron nitride, *Science* **372**, 1458 (2021).
- [7] X. Wang, K. Yasuda, Y. Zhang, S. Liu, K. Watanabe, T. Taniguchi, J. Hone, L. Fu, and P. Jarillo-Herrero, Interfacial ferroelectricity in rhombohedral-stacked bilayer transition metal dichalcogenides, *Nat. Nanotechnol.* **17**, 367 (2022).
- [8] L. Li and M. Wu, Binary compound bilayer and multilayer with vertical polarizations: Two-dimensional ferroelectrics, multiferroics, and nanogenerators, *ACS Nano* **11**, 6382 (2017).
- [9] J. Xiao *et al.*, Berry curvature memory through electrically driven stacking transitions, *Nat. Phys.* **16**, 1028 (2020).
- [10] H. P. Hughes and R. H. Friend, Electrical resistivity anomaly in β -MoTe₂ (Metallic Behaviour), *J. Phys. C: Solid State Phys.* **11**, L103 (1978).
- [11] K. Zhang, C. Bao, Q. Gu, X. Ren, H. Zhang, K. Deng, Y. Wu, Y. Li, J. Feng, and S. Zhou, Raman signatures of inversion symmetry breaking and structural phase transition in Type-II Weyl semimetal MoTe₂, *Nat. Commun.* **7**, 13552 (2016).
- [12] R. He, S. Zhong, H. H. Kim, G. Ye, Z. Ye, L. Winford, D. McHaffie, I. Rilak, F. Chen, X. Luo, Y. Sun, and A. W. Tsen, Dimensionality-driven orthorhombic MoTe₂ at room temperature, *Phys. Rev. B* **97**, 041410(R) (2018).
- [13] S. Y. Chen, T. Goldstein, D. Venkataraman, A. Ramasubramaniam, and J. Yan, Activation of new Raman modes by inversion symmetry breaking in Type II Weyl semimetal candidate T'-MoTe₂, *Nano Lett.* **16**, 5852 (2016).
- [14] A. Tiwari *et al.*, Giant c-axis nonlinear anomalous Hall effect in T_d-MoTe₂ and WTe₂, *Nat. Commun.* **12**, 2049 (2021).
- [15] D. Yang *et al.*, Spontaneous-polarization-induced photovoltaic effect in rhombohedrally stacked MoS₂, *Nat. Photon.* **16**, 469 (2022).
- [16] T. Ideue, K. Hamamoto, S. Koshikawa, M. Ezawa, S. Shimizu, Y. Kaneko, Y. Tokura, N. Nagaosa, and Y. Iwasa, Bulk rectification effect in a polar semiconductor, *Nat. Phys.* **13**, 578 (2017).
- [17] P. He, C. H. Hsu, S. Shi, K. Cai, J. Wang, Q. Wang, G. Eda, H. Lin, V. M. Pereira, and H. Yang, Nonlinear magnetotransport shaped by Fermi surface topology and convexity, *Nat. Commun.* **10**, 1290 (2019).
- [18] Y. Tokura and N. Nagaosa, Nonreciprocal responses from non-centrosymmetric quantum materials, *Nat. Commun.* **9**, 3740 (2018).
- [19] T. Ideue and Y. Iwasa, Symmetry breaking and nonlinear electric transport in van der Waals nanostructures, *Annu. Rev. Condens. Matter Phys.* **12**, 201 (2021).
- [20] See Supplemental Material at <http://link.aps.org/supplemental/10.1103/PhysRevResearch.5.L022022> for sample fabrication, electrical transport measurement, nonreciprocal transport in a bulk sample, scan rate-thickness variations of temperature derivatives of longitudinal resistivity, estimation of carrier densities, and current-angle dependence of the nonlinear signals.
- [21] M. Sakano, M. S. Bahrmy, H. Tsuji, I. Araya, K. Ikeura, H. Sakai, S. Ishiwata, K. Yaji, K. Kuroda, A. Harasawa, S. Shin, and K. Ishizaka, Observation of spin-polarized bands and domain-dependent Fermi arcs in polar Weyl semimetal MoTe₂, *Phys. Rev. B* **95**, 121101(R) (2017).
- [22] Y. Guo *et al.*, Distinctive in-plane cleavage behaviors of two-dimensional layered materials, *ACS Nano* **10**, 8980 (2016).
- [23] H. Sakai, K. Ikeura, M. S. Bahrmy, N. Ogawa, D. Hashizume, J. Fujioka, Y. Tokura, and S. Ishiwata, Critical enhancement of thermopower in a chemically tuned polar semimetal MoTe₂, *Sci. Adv.* **2**, e1601378 (2016).
- [24] Y. Qi *et al.*, Superconductivity in Weyl semimetal candidate MoTe₂, *Nat. Commun.* **7**, 11038 (2016).
- [25] H. Takahashi, T. Akiba, K. Imura, T. Shiino, K. Deguchi, N. K. Sato, H. Sakai, M. S. Bahrmy, and S. Ishiwata, Anticorrelation between polar lattice instability and superconductivity in the Weyl semimetal candidate MoTe₂, *Phys. Rev. B* **95**, 100501(R) (2017).
- [26] F. T. Huang, S. Joon Lim, S. Singh, J. Kim, L. Zhang, J. W. Kim, M. W. Chu, K. M. Rabe, D. Vanderbilt, and S. W. Cheong, Polar and phase domain walls with conducting interfacial states in a Weyl semimetal MoTe₂, *Nat. Commun.* **10**, 4211 (2019).
- [27] J. L. Hart *et al.*, Emergence of layer stacking disorder in c-axis confined MoTe₂, *arXiv:2210.16390* (2022).
- [28] A. Zhang, X. Ma, C. Liu, R. Lou, Y. Wang, Q. Yu, Y. Wang, T. L. Xia, S. Wang, L. Zhang, X. Wang, C. Chen, and Q. Zhang, Topological phase transition between distinct Weyl semimetal states in MoTe₂, *Phys. Rev. B* **100**, 201107(R) (2019).
- [29] F. C. Chen, H. Y. Lv, X. Luo, W. J. Lu, Q. L. Pei, G. T. Lin, Y. Y. Han, X. B. Zhu, W. H. Song, and Y. P. Sun, Extremely large magnetoresistance in the Type-II Weyl semimetal MoTe₂, *Phys. Rev. B* **94**, 235154 (2016).
- [30] Q. Zhou, D. Rhodes, Q. R. Zhang, S. Tang, R. Schönemann, and L. Balicas, Hall effect within the colossal magnetoresistive semimetallic state of MoTe₂, *Phys. Rev. B* **94**, 121101(R) (2016).
- [31] F. C. Chen *et al.*, Planar Hall effect in the Type-II Weyl semimetal T_d-MoTe₂, *Phys. Rev. B* **98**, 041114(R) (2018).
- [32] D. D. Liang *et al.*, Origin of planar Hall effect in Type-II Weyl semimetal MoTe₂, *AIP Adv.* **9**, 055015 (2019).
- [33] S. Lee, J. Jang, S. il Kim, S. G. Jung, J. Kim, S. Cho, S. W. Kim, J. Y. Rhee, K. S. Park, and T. Park, Origin of extremely large magnetoresistance in the candidate Type-II Weyl semimetal MoTe_{2-x}, *Sci. Rep.* **8**, 13937 (2018).
- [34] S. Lim, C. R. Rajamathi, V. Süß, C. Felser, and A. Kapitulnik, Temperature-induced inversion of the spin-photogalvanic effect in WTe₂ and MoTe₂, *Phys. Rev. B* **98**, 121301(R) (2018).
- [35] D. Rhodes, R. Schonemann, N. Aryal, Q. Zhou, Q. R. Zhang, E. Kampert, Y. C. Chiu, Y. Lai, Y. Shimura, G. T. McCandless *et al.*, Bulk Fermi surface of the Weyl Type-II semimetallic candidate γ -MoTe₂, *Phys. Rev. B* **96**, 165134 (2017).
- [36] C. Z. Li, J. G. Li, L. X. Wang, L. Zhang, J. M. Zhang, D. Yu, and Z. M. Liao, Two-carrier transport induced Hall anomaly and large tunable magnetoresistance in Dirac semimetal Cd₃As₂ nanoplates, *ACS Nano* **10**, 6020 (2016).
- [37] P. M. C. Rourke, A. F. Bangura, C. Proust, J. Levallois, N. Doiron-Leyraud, D. LeBoeuf, L. Taillefer, S. Adachi, M. L. Sutherland, and N. E. Hussey, Fermi-surface reconstruction and two-carrier model for the Hall effect in YBa₂Cu₄O₈, *Phys. Rev. B* **82**, 020514(R) (2010).
- [38] N. Xu *et al.*, Evidence of a Coulomb-Interaction-Induced Lifshitz Transition and Robust Hybrid Weyl Semimetal in T_d-MoTe₂, *Phys. Rev. Lett.* **121**, 136401 (2018).
- [39] Y. Wu, N. H. Jo, M. Ochi, L. Huang, D. Mou, S. L. Bud'Ko, P. Canfield, N. Trivedi, R. Arita, and A. Kaminski, Temperature-Induced Lifshitz Transition in WTe₂, *Phys. Rev. Lett.* **115**, 166602 (2015).